JACS
JOURNAL OF THE AMERICAN CHEMICAL SOCIETY
pubs.acs.org/JACS
Article

Synthesis of Isotypic Giant Polymolybdate Cages for Efficient Photocatalytic C−C Coupling Reactions

Jiao-Min Lin,[#] Zhi-Bin Mei,[#] Chenxing Guo,[#] Jun-Rong Li, Yi Kuang, Jing-Wen Shi, Jing-Jing Liu, Xiaopeng Li, Shun-Li Li, Jiang Liu,[*] and Ya-Qian Lan[*]

Cite This: https://doi.org/10.1021/jacs.4c08043

ABSTRACT: The construction of isotypic high-nuclearity inorganic cages with identical pristine parent structure and increasing nuclearity is highly important for molecular growth and structure−property relationship study, yet it still remains a great challenge. Here, we provide an in situ growth approach for successfully synthesizing a series of new giant hollow polymolybdate dodecahedral cages, **Mo$_{250}$**, **Mo$_{260}$-I**, and **Mo$_{260}$-E**, whose structures are growth based on giant polymolybdate cage **Mo$_{240}$**. Remarkably, they show two pathways of nuclear growth based on **Mo$_{240}$**, that is, the growth of 10 and 20 Mo centers on the inner and outer surfaces to afford **Mo$_{250}$** and **Mo$_{260}$-I**, respectively, and the growth of 10 Mo centers both on the inner and outer surfaces to give **Mo$_{260}$-E**. To the best of our knowledge, this is the first study to display the internal and external nuclear growth of a giant hollow polyoxometalate cage. More importantly, regular variations in structure and nuclearity confer these polymolybdate cages with different optical properties, oxidative activities, and hydrogen atom transfer effect, thus allowing them to exhibit moderate to excellent photocatalytic performance in oxidative cross-coupling reactions between different unactivated alkanes and N-heteroarenes. In particular, **Mo$_{240}$** and **Mo$_{260}$-E** with better comprehensive abilities can offer the desired coupling product with yield up to 92% within 1 h.

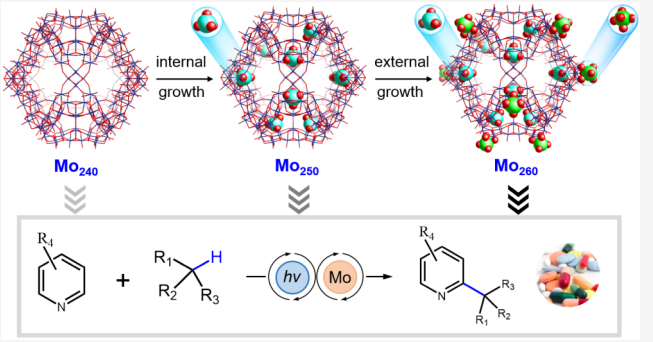

INTRODUCTION

Polyoxometalates (POMs) are a prominent type of discrete early-transition metal-oxo clusters with a diversity of structures and properties.[1−12] In the field of POMs, the synthesis of giant hollow POM cages is interesting and important since they not only have fascinating architectures but also combine the benefits of POM cluster and porous cage; thus, they are highly promising for applications in catalysis, guest recognition, and molecular reactors.[13−19] To date, although a number of giant hollow POM cages, e.g., "hedgehog-like" Mo_{368},[20] truncated icosahedral Mo_{132}[21] and U_{60},[22] pentagonal dodecahedral Mo_{240},[23] have been successfully explored by chemists, there is still a lack of an effective strategy in the synthesis for guiding researchers to explore more derivatives or homologs. From the synthesis experiences of traditional POMs, molecular growth based on some known POMs seems to be a good idea for constructing more POM derivatives.[24−29] In particular, it is even possible to synthesize a series of derivatives that possess identical main skeleton with the pristine parent POMs.[28−30] Such POM derivatives not only largely enrich the structures and properties of traditional POMs but also provide a unique platform for studying their structural transformation process as well as the structure−property relationships.[30−32] In this context, the construction of a series of isotypic giant POM cages that can maintain the pristine parent structure and large opening cavities by a molecular growth approach is very interesting and important, but reports on this breakthrough have not been found so far.

In theory, to achieve molecular growth based on one known giant hollow POM cage, there are two feasible approaches: post growth and in situ growth.[32−34] The post growth approach is to synthesize the parent giant hollow POM cage first and then utilize it as one of the raw materials for further synthesis. In this case, we may expect the parent POM cage to serve as a template, and more metal-oxo units could orderly or randomly grow at the inner and/or outer surface of this parent skeleton to form different derivatives. In contrast, the in situ growth approach is to modify the original reaction conditions under the requirement of maintaining the formation of the parent POM cage, that is, not to completely disrupt the original synthesis conditions. For example, the anions and/or

Received: June 14, 2024
Revised: July 18, 2024
Accepted: July 22, 2024

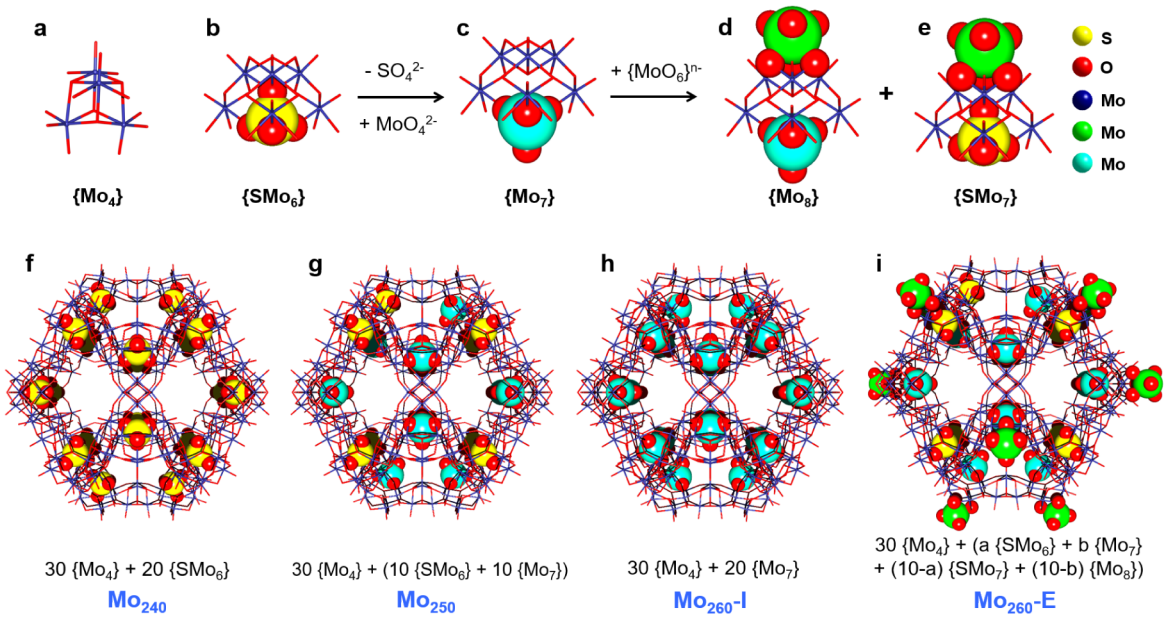

Figure 1. Crystal structures of Mo_{240}, Mo_{250}, Mo_{260}-I, and Mo_{260}-E. (a–e) Ball-and-stick views of the cubane-type edge BB {Mo_4} and the tripod-shaped vertex BBs {SMo_6}, {Mo_7}, {Mo_8}, and {SMo_7}. (f-i) Ball-and-stick views of the assembly and structures of Mo_{240}, Mo_{250}, Mo_{260}-I, and Mo_{260}-E. The MoO_4^{2-} and SO_4^{2-} anions and the additional [MoO_6] units (compared with Mo_{240}) in/on the tripod-shaped vertex BBs are highlighted in space-filling mode.

the solutions are strategically changed to modify the growth of the metal-oxo units. In this case, we may expect the POM building block (BB) self-assembly to form the parent giant POM cage first and then further growth to form the target derivatives, just as that in the post growth approach, or we can also expect the POM BBs to be modified first and then self-assembly via the original mode to form the target derivatives.

In our previous work, we reported a giant polymolybdate dodecahedral cage Mo_{240}, which is the highest nuclearity and symmetry hollow opening pentagonal dodecahedron reported by far.[23] Based on this, we tried to synthesize and simultaneously find out an effective approach for exploring a series of Mo_{240} derivatives that may grow based on Mo_{240}. With many attempts, we found that no target compound can be obtained using the post growth approach because of the low solubility of the precursor Mo_{240} in the reaction system. Nevertheless, using the in situ growth approach, that is, to modify the anions and the H_2O/CH_3CN solution, we successfully synthesized three new Mo_{240} derivatives, Mo_{250}, Mo_{260}-I, and Mo_{260}-E, which not only possess identical main skeleton with the parent Mo_{240} but also exhibit increasing nuclearity. In view of their crystal structures, these derivatives can all be regarded as products growing from Mo_{240}, for which growing 10 and 20 Mo-metal centers in the inner surface (MoO_4^{2-} replaces the SO_4^{2-}/SO_3^{2-} anion in the vertex BB) afford Mo_{250} and Mo_{260}-I, respectively, while growing 10 Mo-metal centers both on the inner and outer surfaces afford Mo_{260}-E. This is the first study on the internal and external nuclear growth of a giant hollow POM cage. More importantly, through this synthetic regulation, we show that the in situ growth approach is an effective strategy for constructing a series of isotypic giant hollow POM cages with identical parent structures. Electrospray ionization-mass spectrometry and scanning transmission electron microscopy imaging revealed that these polymolybdate cages have high stability. In addition, owing to the variation of their nuclearity, Mo^V/Mo^{VI} ratios, and numbers of SO_4^{2-} anion in the skeleton, these polymolybdate cages display different optical properties, oxidative activities, and hydrogen atom transfer effect. Thus, they were treated as heterogeneous photocatalysts for oxidative cross-coupling reactions between different unactivated alkanes and N-heteroarenes. The results revealed that Mo_{240} and Mo_{260}-E can offer desire coupling product with yield up to 92% within 1 h, which is higher than that of Mo_{250}, Mo_{260}-I, and classic $H_3[P(Mo_3O_{10})_4]$ and $(NH_4)_6Mo_7O_{24}$ because of their more superior photoinduced charge transfer capacity, oxidative activity, and hydrogen atom transfer effect.

RESULTS AND DISCUSSION

The giant hollow polymolybdate dodecahedral cage Mo_{240} reported in our previous work is built up by 20 tripod-shaped $[Mo_6O_{22}(SO_3)]^{n-}/[Mo_6O_{21}(SO_4)]^{n-}$ BBs (as vertex, denoted as {SMo_6}) and 30 cubane-type $[Mo_4O_{16}]^{n-}$ BBs (as edge, denoted as {Mo_4}) (Figure 1a,b and f). The vertex BB {SMo_6} is a lacunary ε-Keggin polymolybdate with a coplanar {Mo_6} unit removed, containing either a tetrahedral μ_6-η^3:η^1:η^1:η^1-SO_4^{2-} anion in its center or a pyramidal μ_3-^{1}:η^1:η^1-SO_3^{2-} anion at its chassis. Considering MoO_4^{2-} anion has similar coordinated modes with that of SO_4^{2-} and SO_3^{2-}, it may serve as an anion for replacing the SO_4^{2-}/SO_3^{2-} in the vertex BB {SMo_6} and thus may be able to construct isomorphic polymolybdate cage with higher nuclearity (in this case, the additional Mo-centers may grow on the cage inner surface). In addition, the Mo reduction degree (proportion of Mo^V reaches 75%) of Mo_{240} is much higher than many traditional polymolybdate clusters; thus, it may be able to grow more Mo^{VI} on this cluster when the reaction condition is suitable.

To explore whether Mo_{240} can further grow up to form similar giant cages with higher nuclearity, we used both post growth and in situ growth approaches for the synthesis. In the post growth approach, the Mo_{240} crystals were synthesized first via a hydrothermal reaction between $(NH_4)_6Mo_7O_{24}$, $CoSO_4$,

https://doi.org/10.1021/jacs.4c08043
J. Am. Chem. Soc. XXXX, XXX, XXX–XXX

and $NH_2NH_2{\cdot}2HCl$ in H_2O in the presence of trace dilute H_2SO_4, and then, they were used as one of the raw materials for the further synthesis. It is hoped that the **Mo_{240}** cage could serve as a template and the SO_4^{2-}/SO_3^{2-} anion in the vertex $\{SMo_6\}$ BB may be replaced by the MoO_4^{2-} anion in this process. Besides, more metal-oxo unites may further grow at the inner and/or outer surfaces of this polymolybdate cage. We carried out this reaction through both hydrothermal and conventional synthetic methods. Nevertheless, after a lot of trying, it was still not possible to obtain the target compounds, probably because of the low solubility of **Mo_{240}** in the molybdate solution (although it has moderate solubility in H_2O).

We then used the in situ growth approach for this synthesis. First, to figure out whether the SO_4^{2-}/SO_3^{2-} anion in the vertex $\{SMo_6\}$ BB can be replaced by MoO_4^{2-} anion, the reaction condition of **Mo_{240}** was slightly modified by omitting the use of the $CoSO_4$ and using HCl rather than H_2SO_4 to adjust the pH of the reaction system (Figure S1). After several trials, we successfully synthesized an isomorphic polymolybdate cage with a formula of $(NH_4)_{22}H^+_{52}[H_{60}Mo^V_{180}Mo^{VI}_{60}O_{677}(MoO_4)_{20}]{\bullet}ca276H_2O$ (denoted as **Mo_{260}-I**, Figure 1h), which contains MoO_4^{2-} anion in the vertex BB (denoted as $\{Mo_7\}$, Figure 1c). In this reaction, it was found that keeping similar reaction conditions of **Mo_{240}**, including the reaction temperature, pH, and reducing agent, is important for the synthesis of this isomorphic polymolybdate cage. This is probably because such reaction conditions, especially hydrothermal reaction at high temperature and the presence of reducing agent $NH_2NH_2{\cdot}2HCl$, are helpful for the formation of this high reduction polymolybdate cluster. Considering that both MoO_4^{2-} and SO_4^{2-} can serve as anions for the formation of the vertex BB, we think it may be possible to synthesize other isomorphic polymolybdate cages containing both MoO_4^{2-} and SO_4^{2-} anions. We thus used H_2SO_4 as a pH-adjusting agent. As expected, another isomorphic polymolybdate cage with a formula of $Na_{42}H^+_{18}[H_{60}Mo^V_{180}Mo^{VI}_{60}O_{670}(SO_4)_{10}(MoO_4)_{10}]{\bullet}ca282H_2O$ (denoted as **Mo_{250}**, Figure 1g) was obtained, which contains mixture MoO_4^{2-} and SO_4^{2-} anions in its vertex BBs. It is to be noted that the MoO_4^{2-}/SO_4^{2-} ratio of the resulting crystals could be changed when the concentration of the SO_4^{2-} anion in the reaction system was changed by adding sulfate. To evaluate whether there is other homolog or derivatives of this polymolybdate cage, we further changed the synthesis conditions, such as the reaction temperature and solution. After many trials, it was found that when a small amount of acetonitrile solution was added to the reaction system of **Mo_{250}**, a new isomorphic polymolybdate cage **Mo_{260}-E** (Figure 1i, formula, $Na_{65}H^+_5[H_{50}Mo^V_{180}Mo^{VI}_{70}O_{700}(SO_4)_{10}(MoO_4)_{10}]{\bullet}ca\text{-}(H_2O)_{370}(CH_3CN)_8$) containing more 10 Mo-metal centers in the inner and outer surface, respectively, can be obtained.

Single-crystal X-ray diffraction analysis (SCXRD) reveals that **Mo_{250}**, **Mo_{260}-I**, and **Mo_{260}-E** crystallize in the same cubic space group $Im\bar{3}$ (Table S1), which is consistent with that of **Mo_{240}**. In structure, **Mo_{250}**, **Mo_{260}-I**, and **Mo_{260}-E** possess identical main skeleton with that of **Mo_{240}**, featuring a pentagonal dodecahedron with a large inner cavity (approximately 1.8 nm in diameter) and 12 opening pentagonal windows. As shown in Figure 1b–e, the major difference for the structures between these polymolybdate cages and **Mo_{240}** is localized in the tripod-shaped vertex BBs. Specifically, in the structure of **Mo_{250}**, MoO_4^{2-} anions replace part of the SO_4^{2-}/SO_3^{2-} anions in the vertex BBs (MoO_4^{2-} and SO_4^{2-} anions are disorder in position and their ratio in each **Mo_{250}** cage is approximately 1:1) (Figures 1g and S2–S4), while in **Mo_{260}**, MoO_4^{2-} anions replace all the SO_4^{2-}/SO_3^{2-} anions (Figures 1h and S5). Thus, compared with **Mo_{240}**, **Mo_{250}** and **Mo_{260}-I** have more than 10 and 20 Mo-metal centers, respectively. Because these additional Mo-metal centers are grown on the inner surface of this dodecahedral cage, **Mo_{250}** and **Mo_{260}-I** have quite similar molecular size and lattice volume with that of **Mo_{240}** (Table S1). While in the structure of **Mo_{260}-E**, in addition to the MoO_4^{2-} anions replacing part of the SO_4^{2-}/SO_3^{2-} anions (the ratio of MoO_4^{2-} and SO_4^{2-} is about 1:1), approximately half of the vertex BBs at the outer surface are further coordinated by $[MoO_6]$ units (which are disorder in positions and the occupancy is approximately 0.5) (Figures 1i and S6). Therefore, **Mo_{260}-E** also contains more than 20 Mo-metal centers than **Mo_{240}**. Nevertheless, because half of these additional Mo-metal centers grown on the outer surface of this dodecahedral cage, **Mo_{260}-E** has a larger molecular size and lattice volume than **Mo_{240}** (Table S1).

For these polymolybdate cages, it is interesting that they have similar pentagonal dodecahedral structures and exhibit increased nuclearity and size. Furthermore, in structure, if regarding **Mo_{240}** as a parent structure, **Mo_{250}**, **Mo_{260}-I**, and **Mo_{260}-E** can be considered as derivatives growing from **Mo_{240}**, that is, growing 10 and 20 Mo-metal centers in the inner surface to afford **Mo_{250}** and **Mo_{260}-I**, respectively, while growing 10 Mo-metal centers both on the inner and outer surfaces to form **Mo_{260}-E**. This suggests that in situ growth is an effective approach for synthesizing a series of isotypic giant POM cages with identical pristine parent structure and increasing nuclearity. It is to be noted that although molecular growth based on some known POMs has been reported in the field of traditional POMs, there is still a void among high-nuclearity POM cages. To the best of our knowledge, this is the first study to report the internal and external molecular growth of a giant hollow POM cage.

Bond valence sum (BVS) values and X-ray photoelectron spectrum (XPS) reveal that the oxidation states of the Mo atom in **Mo_{250}**, **Mo_{260}-I** and **Mo_{260}-E** are +5 and +6 (Tables S2–S4 and Figures S7–S9). Furthermore, all three compounds contain 180 Mo^V atoms, for which 120 Mo^V atoms are from the 20 tripod-shaped vertex BBs (the $\{Mo_7\}/\{SMo_7\}/\{Mo_8\}$ BBs, Figure 1c-e) and 60 Mo^V atoms are from the 30 cubane-type $\{Mo_4\}$ BBs (which contain two Mo^V and two Mo^{VI} atoms). These are consistent with those of **Mo_{240}**. In other words, compared with the parent **Mo_{240}**, the additional Mo centers for **Mo_{250}**, **Mo_{260}-I** and **Mo_{260}-E** are all Mo^{VI}. The Mo reduction degrees (proportion of Mo^V) for **Mo_{240}**, **Mo_{250}**, **Mo_{260}-I**, and **Mo_{260}-E** were calculated to be 75.0%, 73.5%, 69.2%, and 69.2%, respectively. Such high Mo reduction degree, associated with the red color of these compounds, suggests that they all belong to Molybdenum Reds (Mo^V content >50%).[23,35] It is to be noted that Molybdenum Reds are a new subclass of polyoxometalate clusters, following the Molybdenum Blues (Mo^V content approximately 35%) and Molybdenum Browns (Mo^V content approximately 45%).[14,36] The reported structures of this family are still relatively rare, and to our knowledge, these polymolybdate cages belong to the highest nuclear Molybdenum Reds reported by far. The phase purity of the as-synthesized samples of these polymolybdate clusters was confirmed by powder XRD

https://doi.org/10.1021/jacs.4c08043
J. Am. Chem. Soc. XXXX, XXX, XXX−XXX

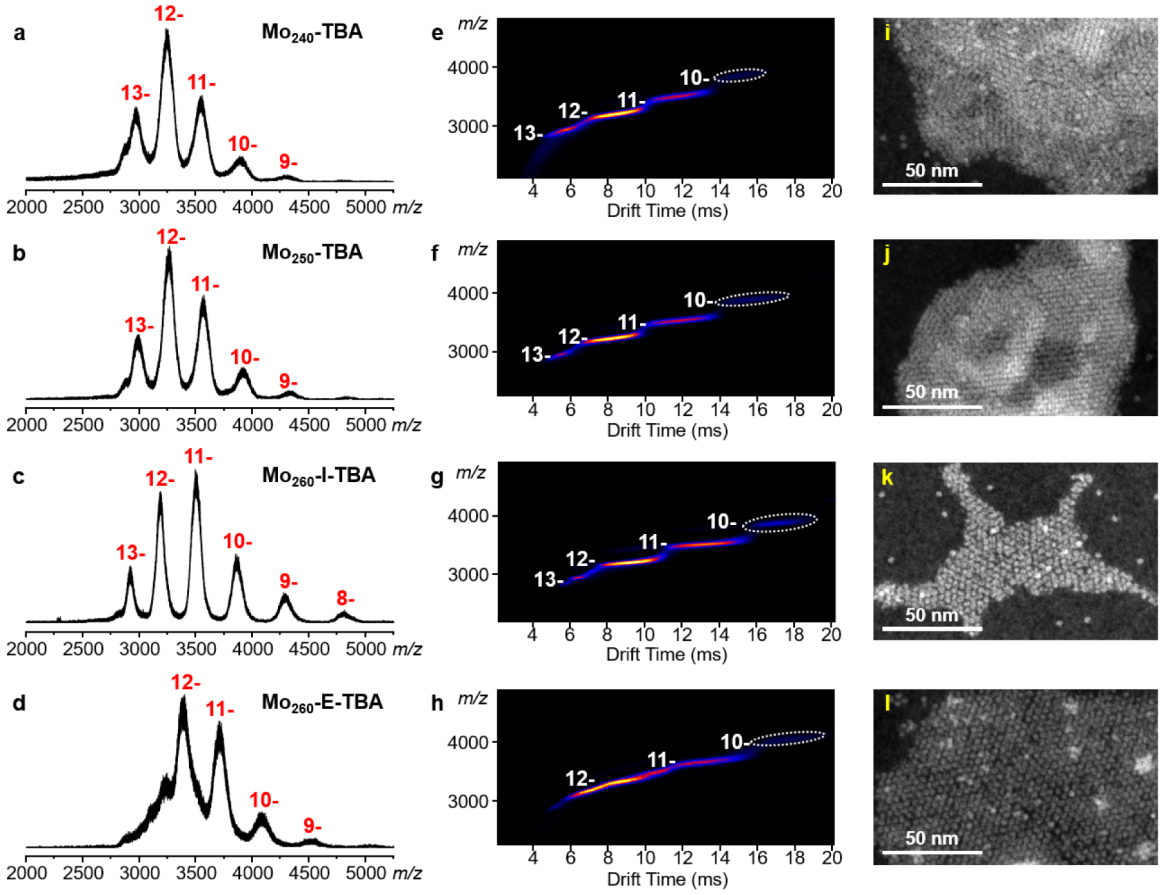

Figure 2. MS and STEM evaluate the stability of giant polymolybdate cages. (a–d) ESI-MS, and (e–h) TWIM-MS plots (m/z vs drift time) of **Mo_{240}-TBA**, **Mo_{250}-TBA**, **Mo_{260}-I-TBA**, and **Mo_{260}-E-TBA** in CH_3CN. (i–l) Dark-field STEM images of **Mo_{240}-TBA**, **Mo_{250}-TBA**, **Mo_{260}-I-TBA**, and **Mo_{260}-E-TBA**.

(Figures S10–S13). Thermogravimetric analysis (TGA) revealed that they exhibit guest molecule loss around 25 to 150 °C and then have a smooth platform up to 750 °C (Figure S14), suggesting they have good thermostability. The FT-IR spectra of these polymolybdate clusters exhibit characteristic bands around 558–957 cm^{-1} for the stretching and stretching vibrations of Mo═O bands and Mo–O–Mo bridges (Figure S15). The UV–visible spectra of these polymolybdate clusters in H_2O show similar absorption peaks around 260 and 310 nm (Figure S16), which are consistent with the characteristic absorption of Molybdenum Red clusters.

The stability of giant POM cages is of great concern since it is critical for their further application. We investigated the stability of these polymolybdate cages using electrospray ionization-mass spectrometry (ESI-MS), traveling-wave ion mobility-mass spectrometry (TWIM-MS), and scanning transmission electron microscopy (STEM). Because these polymolybdate cages show moderate solubility in H_2O but low solubility in organic solutions such as alcohol and acetonitrile, to prepare the samples that suitable for these measurements, the tetrabutylammonium (TBA) salt of these polymolybdate cages were synthesized via reaction with TBA·Br in H_2O (see Supporting Information for details). The resulting TBA salts (denoted as **Mo_{240}-TBA**, **Mo_{250}-TBA**, **Mo_{260}-I-TBA**, and **Mo_{260}-E-TBA**, respectively) show good solubility in acetonitrile. The FT-IR spectra of these polymolybdate cage salts contain the characteristic peaks of TBA, demonstrating the presence of TBA in these samples (Figure S17).

ESI-MS and TWIM-MS are powerful tools for studying the stability of discrete molecular cages/clusters in solution.[37−39] The **Mo_{240}-TBA**, **Mo_{250}-TBA**, **Mo_{260}-I-TBA**, and **Mo_{260}-E-TBA** are dissolved in acetonitrile, respectively, and then investigated by ESI-MS and TWIM-MS. As shown in Figure 2a–d, the ESI-MS spectra of all four compounds consist of a single series of broad peaks covering a range of charge states, including −13 to −9 for **Mo_{240}-TBA** and **Mo_{250}-TBA**, −13 to −8 for **Mo_{260}-I-TBA**, and −12 to −9 for **Mo_{260}-E-TBA**, respectively. Although the peaks for each charge state are broad due to the association of a range of counterions and solvent molecules for such large polymolybdate clusters (which is typical in the ESI-MS of large POMs),[39,40] the single series of peaks indicate that only one major structure is present in each case. Additionally, the TWIM-MS spectra of these polymolybdate cages display a single distribution for the signal at each charge state (Figure 2e–h), further confirming that they remain intact and are highly stable in solution. Notably, owing to the large molecular weight, high negative charge, and usually not very stable under MS detect condition, it still remains a great challenge to measure the MS of large POMs, especially for giant hollow POM cages. To our knowledge, this work represents the first example to evaluate the stability of giant polymolybdate cages with molecular weight up to 35 kDa using ESI-MS and TWIM-MS.

Based on the ESI-MS spectra, the molecular species of these polymolybdate cages at each charge state are deduced (Figures S18–S21 and Tables S5–S8). After deconvolution, the average

https://doi.org/10.1021/jacs.4c08043
J. Am. Chem. Soc. XXXX, XXX, XXX−XXX

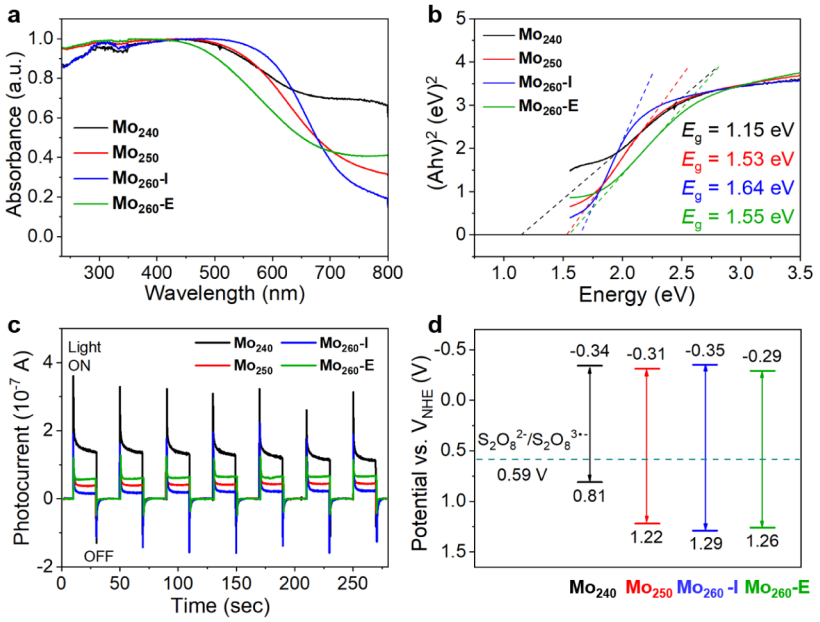

Figure 3. (a) UV−visible diffuse reflection spectra of **Mo_{240}**, **Mo_{250}**, **Mo_{260}-I**, and **Mo_{260}-E** samples. (b) Tauc plots of **Mo_{240}**, **Mo_{250}**, **Mo_{260}-I**, and **Mo_{260}-E** samples. (c) Transient photocurrent response of **Mo_{240}**, **Mo_{250}**, **Mo_{260}-I**, and **Mo_{260}-E** samples under Xe lamp irradiation. (d) Energy band diagrams of **Mo_{240}**, **Mo_{250}**, **Mo_{260}-I**, and **Mo_{260}-E** samples.

molar mass of the intact species of **Mo_{240}-TBA**, **Mo_{250}-TBA**, **Mo_{260}-I-TBA**, and **Mo_{260}-E-TBA** is determined as 41 666, 42 049, 41 094, and 43 679 Da, respectively, which corresponds to the molecular formula of $[H_{60}Mo_{240}O_{674}(SO_3)_{14}(SO_4)_6](TBA)_{20}H_{48}(H_2O)_{12}(CH_3CN)_{24}$, $[H_{60}Mo_{240}O_{670}(SO_4)_{10}(MoO_4)_{10}](TBA)_{19}H_{41}(H_2O)_{12}(CH_3CN)_{20}$, $[H_{60}Mo_{240}O_{677}(MoO_4)_{20}](TBA)_{15}H_{59}(H_2O)_2(CH_3CN)_6$, and $[H_{50}Mo_{250}(SO_4)_{10}(MoO_4)_{10}O_{700}](TBA)_{21}H_{49}(H_2O)_7(CH_3CN)_{15}$, respectively. It is to be noted that because the signal peak for each charge state in the ESI-MS is quite broad, these estimated molar mass and formulas are fairly coarse.

To further demonstrate the stability of these polymolybdate cages, STEM images were characterized. The **Mo_{240}-TBA**, **Mo_{250}-TBA**, **Mo_{260}-I-TBA**, and **Mo_{260}-E-TBA** were dissolved in acetonitrile, respectively, and then, the acetonitrile solution was dropped onto the lacey carbon-coated Cu grid. After the acetonitrile was evaporated under an ambient atmosphere, the lacey carbon-coated Cu grid was used for STEM imaging. As shown in Figures 2i−l and S22, similar bright dots with uniform size distribution were observed for the samples of **Mo_{240}-TBA**, **Mo_{250}-TBA**, **Mo_{260}-I-TBA**, and **Mo_{260}-E-TBA**. The sizes of the bright dots are around 3.2 ± 0.2 nm, which are comparable to those of their crystal structures, suggesting that these giant polymolybdate cages have good stability. Interestingly, in these STEM images, many bright dots forming regular 2D array on the lacey carbon-coated Cu grid can also be observed, which indicate that these polymolybdate cages may further self-assemble into 2D superstructures.

Molybdenum Reds, as a new subclass of POMs, and their properties and applications are still poorly explored. Because **Mo_{240}**, **Mo_{250}**, **Mo_{260}-I**, and **Mo_{260}-E** (belong to Molybdenum Reds) have high Mo reduction degree and their crystals exhibit deep red color, we think they may have good light absorption capacity and can be used as photocatalysts. Therefore, we investigated their optical properties first. The solid-state UV−visible absorption spectra of **Mo_{240}**, **Mo_{250}**, **Mo_{260}-I**, and **Mo_{260}-E** reveal that they have significant absorption bands around 500, 500, 550, and 450 nm, respectively (Figure 3a). Furthermore, their absorption bands can be extended to 800 nm, indicating that they have good light absorption ability. In comparison, **Mo_{240}** exhibits the best light absorption, following **Mo_{260}-I**, **Mo_{250}**, and **Mo_{260}-E**, which is probably because of their difference in the Mo reduction degree.[35] The optical band gap (E_g) of **Mo_{240}**, **Mo_{250}**, **Mo_{260}-I**, and **Mo_{260}-E** were calculated using the Kubelka−Munk function and were estimated to be 1.15, 1.53, 1.64, and 1.55 eV through Tauc plots, respectively (Figure 3b). In order to calculate the energy band distribution of these three compounds, the Mott−Schottky electrochemical measurements were carried out at 500, 1000, and 1500 Hz frequencies, respectively. The results reveal that the lowest unoccupied molecular orbital (LUMO) positions of **Mo_{240}**, **Mo_{250}**, **Mo_{260}-I**, and **Mo_{260}-E** were estimated to be −0.34, −0.31, −0.35, and −0.29 V vs NHE (pH = 7), respectively (Figure S23), indicating that they have semiconductor behaviors. Based on this, the highest-occupied molecular orbital (HOMO) positions were calculated and converted to electrochemical energy potentials in volts vs normal hydrogen electrode (NHE) as 0.81, 1.22, 1.29, and 1.26 V for **Mo_{240}**, **Mo_{250}**, **Mo_{260}-I**, and **Mo_{260}-E**, respectively (Figure 3d). These results indicate that these polymolybdate cages have similar reducing activity but different oxidative activity (following the order of **Mo_{260}-I** > **Mo_{260}-E** > **Mo_{250}**> **Mo_{240}**). We then investigated the separation capability of photogenerated electron−hole pairs of these clusters by transient photocurrent measurement. As displayed in Figure 3c, in comparison, **Mo_{240}** and **Mo_{260}-E** exhibit better photocurrent intensity than **Mo_{250}** and **Mo_{260}-I**, indicating that they have better photogenerated charge separation and transfer capacity under the analogous conditions.

Considering that these polymolybdate clusters have good UV−vis light adsorption and photoinduced charge transfer properties, they may serve as photocatalysts. Therefore, we investigated the catalytic activity of these polymolybdate cages for the photocatalyzed oxidative cross-coupling reaction

https://doi.org/10.1021/jacs.4c08043
J. Am. Chem. Soc. XXXX, XXX, XXX−XXX

between unactivated alkanes and heteroarenes. This oxidative cross-coupling reaction has attracted great interest in recent years because of its high atom economy and the importance of functionalized N-heteroarenes in medicines and materials, but it is a long-pending issue since it involves the activation of inert C(sp^3)-H bonds and the coupling of C−C bond.[41−44] Previous study has revealed that this cross-coupling reaction usually involved two steps.[43,44] The first step is the photocatalyzed activation of the hydrogen atom transfer (HAT) reagent to abstract the hydrogen atom of the alkane to form an alkyl radical, which will further react with the N-heteroarene to generate an amine cation radical intermediate. The second step is that the amine cation radical intermediate would be oxidized by the activated catalyst through a single-electron transfer (SET) process to form the desired product and regenerate the catalyst. Thus, for this photocatalytic reaction, except for the light adsorption and photoinduced charge-transfer capacity, the redox activity of the photocatalyst is also crucial.

The cross-coupling between cyclohexane (1a) and methyl isoquinoline-3-carboxylate (2a) to form methyl 1-cyclohexylisoquinoline-3-carboxylate (3a) was employed as the original reaction for screening the reaction conditions (Table 1).

Table 1. Optimization of the Reaction Condition

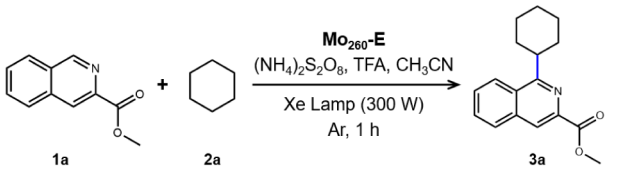

entry	deviation from the standard conditions[a]	yield of 3a (%)[b]
1	standard condition	92
2	no light	n.d
3	no **Mo_{260}-E**	9
4	no $(NH_4)_2S_2O_8$	24
5	no TFA	26
6	1 equiv. TFA	40
7	4 equiv. TFA	50
8	1 equiv. $(NH_4)_2S_2O_8$	18
9	4 equiv. $(NH_4)_2S_2O_8$	37
10	$K_2S_2O_8$ instead of $(NH_4)_2S_2O_8$	55
11	NaS_2O_8 instead of $(NH_4)_2S_2O_8$	62
12	**Mo_{240}** instead of **Mo_{260}-E**	95
13	**Mo_{250}** instead of **Mo_{260}-E**	87
14	**Mo_{260}-I** instead of **Mo_{260}-E**	48
15	$H_3[PMo_{12}O_{40}]$ instead of **Mo_{260}-E**	19
16	$(NH_4)_6Mo_7O_{24}$ instead of **Mo_{260}-E**	12

[a]Reaction conditions: 1a (0.03 mmol), 2a (0.4 mL), **Mo_{260}-E** (10.0 mg), $(NH_4)_2S_2O_8$ (0.06 mmol), trifluoroacetic acid (TFA, 0.06 mmol), CH_3CN (1.6 mL), Xe lamp (wavelength around 300−800 nm), Ar atmosphere, room temperature, 1 h. [b]Isolated yield.

Because **Mo_{260}-E** can be synthesized in higher yield than the other three polymolybdate clusters, we thus investigated its catalytic activation first. The result revealed that the yield of product 3a can reach 92% when using **Mo_{260}-E** as the catalyst in the presence of a protonation reagent trifluoroacetic acid (TFA) (2 equiv) and an oxidant $(NH_4)_2S_2O_8$ (2 equiv) in acetonitrile under Ar atmosphere and Xenon lamp (300 W) irradiation for 1 h (Table 1, entry 1). Control experiments showed that light irradiation **Mo_{260}-E**, TFA, and $(NH_4)_2S_2O_8$ is indispensable for this reaction. Without light irradiation, almost negligible 3a product can be detected, while without **Mo_{260}-E**, $(NH_4)_2S_2O_8$, and TFA, the yield of 3a is only 9%, 24%, and 26%, respectively (Table 1, entries 2−5). In addition, a lower catalyst loading of 5.0 mg led to a lower 3a yield of 53%. Lowing or increasing the equivalents of TFA to 1 and 4, the yield of 3a dropped to 40% and 50% (Table 1, entries 6 and 7), respectively, while lowering or increasing the equivalents of the terminal oxidant $(NH_4)_2S_2O_8$ to approximately 1 and 4, the yield of 3a dropped to 18% and 37% (Table 1, entries 8 and 9), respectively. Moreover, changing $(NH_4)_2S_2O_8$ to $K_2S_2O_8$ or $Na_2S_2O_8$, the product of 3a is also dropped to 55% and 62% (Table 1, entries 10 and 11), respectively, suggesting $(NH_4)_2S_2O_8$ is a better oxidant for this reaction.

Based on the above optimal reaction conditions, we further investigated the photocatalytic performance of **Mo_{240}**, **Mo_{250}**, and **Mo_{260}-I** for this model reaction. The results revealed that the yield of 3a was approximately 95% for **Mo_{240}**, 87% for **Mo_{250}** and 48% for **Mo_{260}-I**, respectively (Table 1, entries 12−14). These results suggest that **Mo_{240}** has the best catalytic performance for this reaction, following **Mo_{260}-E**, **Mo_{250}**, and **Mo_{260}-I**. This is probably because **Mo_{240}** has better performance both in light absorption and photoinduced charge transfer. While for **Mo_{260}-E**, because of its higher oxidative activity, it may have higher catalytic activity for the oxidation of the amine cation radical intermediate in the second step and thus shows better catalytic activity in this reaction than **Mo_{250}** and **Mo_{260}-I**. On the whole, both **Mo_{240}** and **Mo_{260}-E** can offer 3a yield up to 90% within 1 h, suggesting they can serve as excellent photoredox catalysts for this reaction. To further compare the catalytic performances of **Mo_{240}** and **Mo_{260}-E**, we determined the time-dependent yield of 3a. The results revealed that the yields of 3a are similar for **Mo_{240}** and **Mo_{260}-E** under the same reaction time (Figure S24), suggesting that they indeed have comparable catalytic performances. As a comparison, we also investigated the classic phosphomolybdic acid cluster $H_3[P(Mo_3O_{10})_4]$ and hexaammonium molybdate $(NH_4)_6Mo_7O_{24}$, whose Mo metals are all +6 oxidation state, as photocatalysts for this model reaction under the identical reaction conditions. The results revealed that the 3a yields are only 19% and 12% for $H_3[P(Mo_3O_{10})_4]$ and $(NH_4)_6Mo_7O_{24}$ (Table 1, entries 15 and 16), respectively, verifying the better photocatalytic activity of our polymolybdate clusters.

Encouraged by the high catalytic performance and facile synthesis of **Mo_{260}-E**, we then investigated its generality for this photocatalytic oxidative cross-coupling reaction between alkanes and heteroarenes. As summarized in Table 2, isoquinoline derivatives with cyano group can also react selectively with cyclohexane at its most electron-poor positions, yielding the corresponding cyclohexyl product (3b) with a yield of 99% after 2h of reaction. Moreover, medicinal-related N-heteroarene molecules such as phenanthridine and 2,6-diphenylpyridine are also feasible under these conditions, and the yield of corresponding cyclohexyl products (3c and 3d) can reach 92% and 99% within 1 and 2 h, respectively. Excepting N-heteroarenes, we also explored the scope of alkanes in this reaction system. As summarized in Table 2, other cycloparaffins, such as cycloheptane, cyclooctane, and even adamantine, can also react smoothly with methyl isoquinoline-3-carboxylate to give corresponding products 3e, 3f, and 3g with yields of 83%, 98%, and 87% at 1−2 h, respectively. Besides, tetrahydropyran can also react

https://doi.org/10.1021/jacs.4c08043
J. Am. Chem. Soc. XXXX, XXX, XXX−XXX

Table 2. Substrate Scope for Photocatalytic Reactions[ab]

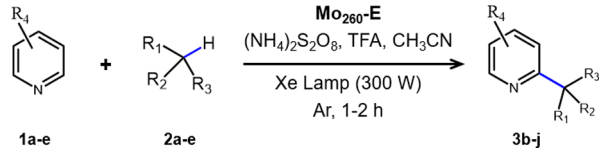

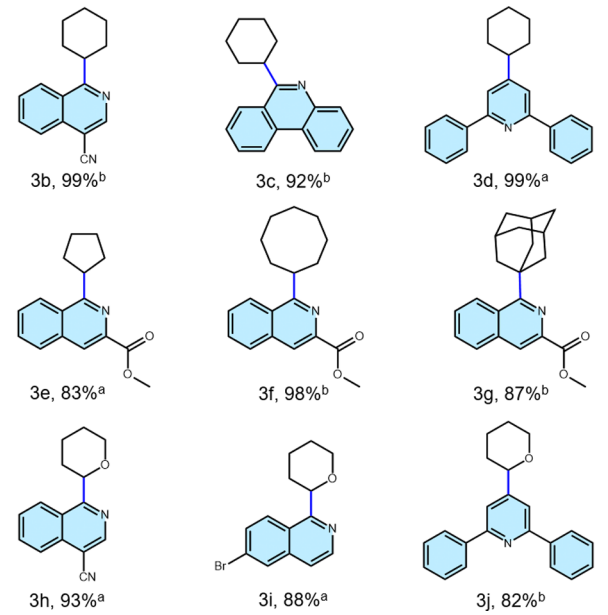

[a]Reaction under standard condition. [b]Reaction for 2 h.

with different N-heteroarenes to give products of 3h, 3i, and 3j with yields of 93%, 88%, and 82% at 1−2 h. These results suggest that **Mo_{260}-E** is indeed a promising photocatalyst for accomplishing this oxidative coupling reaction.

After the photocatalytic reactions, catalyst **Mo_{260}-E** did not dissolve, suggesting the nature of heterogeneous catalysis. To confirm this, the solid sample after the photocatalytic reaction was filtrated, and the filtrate was characterized by inductive coupled plasma (ICP), while the solid was characterized by infrared (IR) spectrum. The ICP results revealed that the residual catalyst in the filtrate is only approximately 0.017% (Table S9), which is almost negligible, confirming the heterogeneous catalytic nature of **Mo_{260}-E**. In addition, the solid IR spectra of the sample before and after photocatalytic reaction are nearly unchanged (Figure S25), indicating its structural stability. We then evaluated the reusability of **Mo_{260}-E** by cyclic photocatalytic experiments. The sample after each photocatalytic run was recovered by centrifugation and washed with acetonitrile, and then, the recovered sample was subsequently employed in the next catalytic run. The results revealed that **Mo_{260}-E** can maintain 86% of its initial catalytic activity after four cycles of reuse (Figure S26), indicating that it has good stability and reusability for this photocatalytic reaction.

The reaction mechanism of this photocatalytic C−C coupling reaction was then investigated. According to previous study, this reaction usually involved two steps, including the generation of the alkyl radical and the oxidation of the amine cation radical intermediate.[43,44] Generally, the generation of the alkyl radical is achieved through the HAT path with sulfate radical as HAT agent. In this reaction system, we think that the

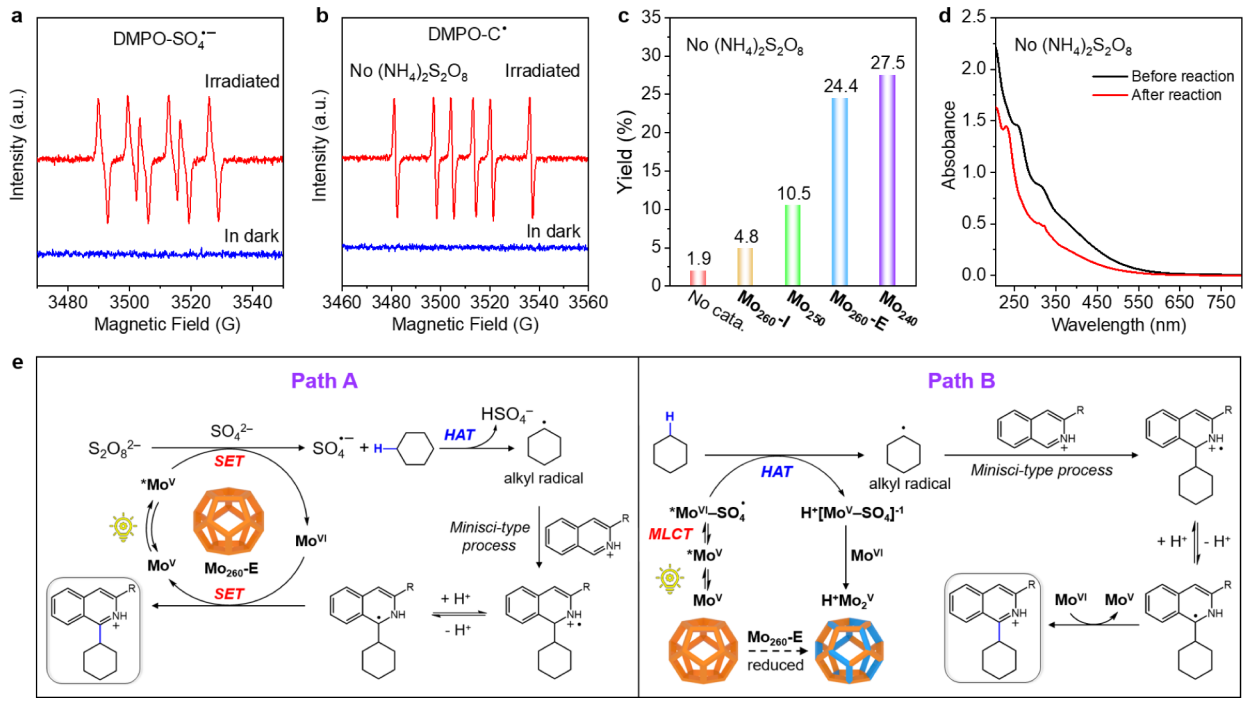

Figure 4. Mechanism of photocatalytic C−C coupling reaction with **Mo_{260}-E**. (a) ESR signals of the reaction solution with **Mo_{260}-E** in darkness and under light irradiation in the presence of DMPO as the spin-trapping reagent. (b) ESR signals of the reaction solution with **Mo_{260}-E** but without $(NH_4)_2S_2O_8$ in darkness and under light irradiation in the presence of DMPO as the spin-trapping reagent. (c) Yield of 3a for the photocatalytic reaction for **Mo_{240}**, **Mo_{250}**, **Mo_{260}-I**, and **Mo_{260}-E** under standard conditions but without $(NH_4)_2S_2O_8$. (d) UV−visible absorption spectra of **Mo_{260}-E** in aqueous solution before and after the photocatalytic reaction without $(NH_4)_2S_2O_8$. (e) Two proposed mechanisms of the photocatalytic C−C coupling reaction in this work.

https://doi.org/10.1021/jacs.4c08043
J. Am. Chem. Soc. XXXX, XXX, XXX−XXX

sulfate radical may be generated from $(NH_4)_2S_2O_8$ or from the SO_4^{2-} anion in the skeleton of the polymolybdate cage. First, we carried out controlled experiments under the standard conditions by adding (2,2,6,6-tetramethylpiperidin-1-yl)oxyl (TEMPO) as a radical scavenger. The result revealed that the yield of the coupling product dropped significantly to approximately 6%, suggesting that this reaction follows a radical pathway (Figure S27). We then used EPR spectroscopy (with DMPO as a spin-trapping reagent) to confirm the generation of sulfate radical in the reaction system upon light irradiation. As shown in Figure 4a, before excitation, the EPR signal of the reaction system is silent, while after continuous irradiation for 10 min, a vigorous EPR signal that corresponds to the sulfate radical can be observed, suggesting the generation of sulfate radical in the reaction system after light irradiation.

To demonstrate that the SO_4^{2-} anion in the skeleton of these polymolybdate cages can also form sulfate radical for abstracting hydrogen atom from cyclohexane 2a to generate cyclohexyl radical, we used EPR spectroscopy to capture the carbon radical signal (with DMPO as a spin-trapping reagent) for the reaction system under standard conditions but without $(NH_4)_2S_2O_8$. As shown in Figure 4b, before light irradiation, the EPR signals are silent, while after light irradiation for 10 min, a vigorous EPR signal that corresponds to the carbon radical can be observed, suggesting that **Mo_{260}-E** can act as a HAT agent for promoting the alkane to generate alkyl radical upon light irradiation. In addition, controlled experiments that were carried out under the standard conditions but without $(NH_4)_2S_2O_8$ revealed that the yields of 3a were approximately 27.5% for **Mo_{240}** (contains 20 SO_4^{2-} anions), 10.5% for **Mo_{250}** (contains 10 SO_4^{2-} anions), 4.8% for **Mo_{260}-I** (without SO_4^{2-} anions), and 24.4% for **Mo_{260}-E** (contains 10 SO_4^{2-} anions) (Figure 4c), which is consistent with the number of SO_4^{2-} anions in their skeleton. It is to be noted that the yield of 3a for **Mo_{260}-I** without SO_4^{2-} anions is similar to the control group without catalyst and $(NH_4)_2S_2O_8$ (Figure 4c), suggesting that the HAT effect should originate from the SO_4^{2-} anion rather than the polymolybdates.

Based on the above experiments and previous reports, two plausible reaction mechanisms were proposed. As shown in Figure 4e, path A, under light irradiation, the Mo^V atom in the photocatalyst polymolybdate cage is excited to its photoexcited state $*Mo^V$, followed by a single electron transfer from $*Mo^V$ to furnish Mo^{VI} and sulfate radical anion. Subsequently, the sulfate radical anion abstracts an H atom from cyclohexane to generate a cyclohexyl radical, which possesses enough nucleophilicity to undergo the Minisci-type reaction with the protonated electron-deficient heteroarene, leading to the formation of the amine radical cation. Then, this amine radical cation loses a proton to give α-amino radical. Finally, this α-amino radical would be further oxidized by Mo^{VI} to offer the desired product and regenerate the photocatalyst. Because **Mo_{240}** and **Mo_{260}-E** have better photoinduced charge transfer capacity and higher oxidative activity (Figure 3c,d), respectively, they have better performance in the photoinduced generation of sulfate radical anion and in the oxidation of the α-amino radical, thus displaying better photocatalytic performance in this reaction.

As a small amount of 3a product can also be observed when this reaction was carried out in the absence of oxidant $(NH_4)_2S_2O_8$, we think that there is another reaction path that utilized the photocatalyst polymolybdate cage as an oxidant for this reaction. As shown in Figure 4e, path B, upon light irradiation, the Mo^V atom in the polymolybdate cage is excited to its photoexcited state $*Mo^V$. Then, an electron is transferred from $*Mo^V$ to its adjacent coordination SO_4^{2-} anion to offer $*Mo^{VI}-SO_4\bullet$. This $*Mo^{VI}-SO_4\bullet$ would abstract an H atom from cyclohexane to form a cyclohexyl radical and $H^+[Mo^V-SO_4]^{-1}$. Subsequently, similar to that in path A, the cyclohexyl radical reacts with the N-heteroarene, resulting the α-amino radical, which will be further oxidized to offer the desired product. In this reaction path, the oxidant used to oxidize the α-amino radical and $H^+[Mo^V-SO_4]^{-1}$ is the Mo^{VI} atom on the polymolybdate cage. As a result, more Mo^V atoms in the photocatalyst poly(molybdate) cage would be formed after the photocatalytic reaction. The UV−visible absorption spectrum of **Mo_{260}-E** in aqueous solution after photocatalytic reaction (without $(NH_4)_2S_2O_8$) shows obviously blue shift than that before photocatalytic reaction, confirming that more Mo^V atoms in **Mo_{260}-E** after photocatalytic reaction (Figure 4d). As the photocatalyst is unable to be regenerated in this reaction path, only a small amount of product 3a can be observed. Nevertheless, it reveals that the SO_4^{2-} anion coordinated on the polymolybdate cage has a HAT effect for promoting this photocatalytic cross-coupling reaction.

CONCLUSIONS

In summary, we have successfully synthesized a series of new giant hollow polymolybdate dodecahedral cages, **Mo_{250}**, **Mo_{260}-I**, and **Mo_{260}-E**, through an in situ growth approach. In structure, these polymolybdate cages can be regarded as products growing based on polymolybdate cage **Mo_{240}**. Compared with **Mo_{240}**, these polymolybdate cages display both intra- and extracage nuclear growth, which is rarely reported among giant POM cages. This suggests that in situ growth approach can be an effective approach for constructing a series of isotypic giant hollow POM cages with identical parent structures. The stability of these hollow giant polymolybdate cages with molecular weight up to 35 kDa was demonstrated by ESI-MS and TWIM-MS for the first time. In addition, owing to the slight difference in nuclearity, Mo^V/Mo^{VI} ratios, and numbers of SO_4^{2-} anion in the skeletons, these polymolybdate clusters exhibit quite a difference in optical properties, oxidative activities, and hydrogen atom transfer effect, which make them as heterogeneous photocatalysts that display different catalytic performance for the oxidative cross-coupling reaction between unactivated alkanes and N-heteroarenes. This work would shed some light on the synthesis and exploration of photocatalytic applications of giant POM cages.

ASSOCIATED CONTENT

Supporting Information

The Supporting Information is available free of charge at https://pubs.acs.org/doi/10.1021/jacs.4c08043.

Detailed information regarding the experimental methods, characterization analysis, catalytic experiments, and CIF files (PDF)

Accession Codes

CCDC 2351923, 2351924, 2351925 contain the supplementary crystallographic data for this paper. These data can be obtained free of charge via www.ccdc.cam.ac.uk/data_request/cif., or by emailing data_request@ccdc.cam.ac.uk, or by contacting The Cambridge Crystallographic Data Centre, 12

https://doi.org/10.1021/jacs.4c08043
J. Am. Chem. Soc. XXXX, XXX, XXX−XXX

Union Road, Cambridge CB2 1EZ, UK; fax: +44 1223 336 033.

AUTHOR INFORMATION

Corresponding Authors

Jiang Liu − *Guangdong Provincial Key Laboratory of Carbon Dioxide Resource Utilization, School of Chemistry, South China Normal University, Guangzhou, Guangdong 510006, China;* orcid.org/0000-0002-2596-4928; Email: liuj0828@m.scnu.edu.cn

Ya-Qian Lan − *Guangdong Provincial Key Laboratory of Carbon Dioxide Resource Utilization, School of Chemistry, South China Normal University, Guangzhou, Guangdong 510006, China;* orcid.org/0000-0002-2140-7980; Email: yqlan@m.scnu.edu.cn

Authors

Jiao-Min Lin − *Guangdong Provincial Key Laboratory of Carbon Dioxide Resource Utilization, School of Chemistry, South China Normal University, Guangzhou, Guangdong 510006, China*

Zhi-Bin Mei − *Guangdong Provincial Key Laboratory of Carbon Dioxide Resource Utilization, School of Chemistry, South China Normal University, Guangzhou, Guangdong 510006, China*

Chenxing Guo − *College of Chemistry and Environmental Engineering, Shenzhen University, Shenzhen, Guangdong 518060, China; Shenzhen University General Hospital, Shenzhen University Clinical Medical Academy, Shenzhen, Guangdong 518055, China*

Jun-Rong Li − *Guangdong Provincial Key Laboratory of Carbon Dioxide Resource Utilization, School of Chemistry, South China Normal University, Guangzhou, Guangdong 510006, China*

Yi Kuang − *Guangdong Provincial Key Laboratory of Carbon Dioxide Resource Utilization, School of Chemistry, South China Normal University, Guangzhou, Guangdong 510006, China*

Jing-Wen Shi − *Guangdong Provincial Key Laboratory of Carbon Dioxide Resource Utilization, School of Chemistry, South China Normal University, Guangzhou, Guangdong 510006, China*

Jing-Jing Liu − *Guangdong Provincial Key Laboratory of Carbon Dioxide Resource Utilization, School of Chemistry, South China Normal University, Guangzhou, Guangdong 510006, China*

Xiaopeng Li − *College of Chemistry and Environmental Engineering, Shenzhen University, Shenzhen, Guangdong 518060, China; Shenzhen University General Hospital, Shenzhen University Clinical Medical Academy, Shenzhen, Guangdong 518055, China;* orcid.org/0000-0001-9655-9551

Shun-Li Li − *Guangdong Provincial Key Laboratory of Carbon Dioxide Resource Utilization, School of Chemistry, South China Normal University, Guangzhou, Guangdong 510006, China*

Complete contact information is available at: https://pubs.acs.org/10.1021/jacs.4c08043

Author Contributions

#J.-M.L., Z.-B.M., and C.G. contributed equally to this work.

Notes

The authors declare no competing financial interest.

ACKNOWLEDGMENTS

This work was supported by the National Key R&D Program of China (2023YFA1507204 and 2023YFA1507201), the National Natural Science Foundation of China (22225109, 22271104, 22071109, and 22201046), Young Top Talents of Pearl River Talent Program of Guangdong Province (2021QN02L617), and Guangdong Basic and Applied Basic Research Foundation (2023A1515030097 and 2023B1515120060).

REFERENCES

(1) Long, D.-L.; Tsunashima, R.; Cronin, L. Polyoxometalates: Building Blocks for Functional Nanoscale Systems. *Angew. Chem., Int. Ed.* **2010**, *49*, 1736−1758.

(2) Liu, J.-C.; Zhao, J.-W.; Streb, C.; Song, Y.-F. Recent Advances on High-Nuclear Polyoxometalate Clusters. *Coord. Chem. Rev.* **2022**, *471*, 214734.

(3) Gumerova, N. I.; Rompel, A. Synthesis, structures and applications of electron-rich polyoxometalates. *Nat. Rev. Chem.* **2018**, *2*, 0112.

(4) Li, X.-X.; Li, C.-H.; Hou, M.-J.; Zhu, B.; Chen, W.-C.; Sun, C.-Y.; Yuan, Y.; Guan, W.; Qin, C.; Shao, K.-Z.; Wang, X.-L.; Su, Z.-M. Ce-mediated molecular tailoring on gigantic polyoxometalate $\{Mo_{132}\}$ into half-closed $\{Ce_{11}Mo_{96}\}$ for high proton conduction. *Nat. Commun.* **2023**, *14*, 5025.

(5) Zhang, H.; Li, A.; Li, K.; Wang, Z.; Xu, X.; Wang, Y.; Sheridan, M. V.; Hu, H.-S.; Xu, C.; Alekseev, E. V.; Zhang, Z.; Yan, P.; Cao, K.; Chai, Z.; Albrecht-Schönzart, T. E.; Wang, S. Ultrafiltration separation of Am(VI)-polyoxometalate from lanthanides. *Nature* **2023**, *616*, 482−487.

(6) Amthor, S.; Knoll, S.; Heiland, M.; Zedler, L.; Li, C.; Nauroozi, D.; Tobaschus, W.; Mengele, A. K.; Anjass, M.; Schubert, U. S.; Dietzek-Ivanšić, B.; Rau, S.; Streb, C. A photosensitizer−polyoxometalate dyad that enables the decoupling of light and dark reactions for delayed on-demand solar hydrogen production. *Nat. Chem.* **2022**, *14*, 321−327.

(7) Yang, H.; Yang, D.; Zhou, Y.; Wang, X. Polyoxometalate Interlayered Zinc−Metallophthalocyanine Molecular Layer Sandwich as Photocoupled Electrocatalytic CO_2 Reduction Catalyst. *J. Am. Chem. Soc.* **2021**, *143*, 13721−13730.

(8) Suzuki, K.; Mizuno, N.; Yamaguchi, K. Polyoxometalate Photocatalysis for Liquid-Phase Selective Organic Functional Group Transformations. *ACS Catal.* **2018**, *8*, 10809−10825.

(9) Shimoyama, Y.; Ogiwara, N.; Weng, Z.; Uchida, S. Oxygen Evolution Reaction Driven by Charge Transfer from a Cr Complex to Co-Containing Polyoxometalate in a Porous Ionic Crystal. *J. Am. Chem. Soc.* **2022**, *144*, 2980−2986.

(10) Ravelli, D.; Fagnoni, M.; Fukuyama, T.; Nishikawa, T.; Ryu, I. Site-Selective C−H Functionalization by Decatungstate Anion Photocatalysis: Synergistic Control by Polar and Steric Effects Expands the Reaction Scope. *ACS Catal.* **2018**, *8*, 701−713.

(11) Weinstock, I. A.; Schreiber, R. E.; Neumann, R. Dioxygen in Polyoxometalate Mediated Reactions. *Chem. Rev.* **2018**, *118*, 2680−2717.

(12) She, S.; Bell, N. L.; Zheng, D.; Mathieson, J. S.; Castro, M. D.; Long, D.-L.; Koehnke, J.; Cronin, L. Robotic synthesis of peptides containing metal-oxide-based amino acids. *Chem* **2022**, *8*, 2734−2748.

(13) Müller, A.; Gouzerh, P. From Linking of Metal-Oxide Building Blocks in a Dynamic Library to Giant Clusters with Unique Properties and Towards Adaptive Chemistry. *Chem. Soc. Rev.* **2012**, *41*, 7431−7463.

(14) Long, D.-L.; Cronin, L. Advances in gigantic polyoxomolybdate chemistry. In *Advances in Inorganic Chemistry*, Hubbard, C. D.; van Eldik, R., Eds.; Academic Press, 2021; Vol. *78*, pp. 227267.

(15) Lee, H.-J.; Cho, E. S. Selective Photocatalytic C−C Bond Cleavage of Lignin Models and Conversion to High-Value Chemical

by Polyoxometalate Under a Mild Water-Based Environment. *ACS Sustainable Chem. Eng.* **2023**, *11*, 7624−7632.
(16) Elliott, A.; McAllister, J.; Long, D.-L.; Song, Y.-F.; Miras, H. N. Pore "Softening" and Emergence of Breathability Effects of New Keplerate Nano-Containers. *Angew. Chem., Int. Ed.* **2023**, *62*, No. e202218897.
(17) Zhu, M.; Han, S.; Liu, J.; Tan, M.; Wang, W.; Suzuki, K.; Yin, P.; Xia, D.; Fang, X. $\{Mo_{126}W_{30}\}$: Polyoxometalate Cages Shaped by $\pi-\pi$ Interactions. *Angew. Chem., Int. Ed.* **2022**, *61*, No. e202213910.
(18) Huang, C.; Chai, Y.; Jiang, Y.; Forth, J.; Ashby, P. D.; Arras, M. M. L.; Hong, K.; Smith, G. S.; Yin, P.; Russell, T. P. The Interfacial Assembly of Polyoxometalate Nanoparticle Surfactants. *Nano Lett.* **2018**, *18*, 2525−2529.
(19) Watfa, N.; Melgar, D.; Haouas, M.; Taulelle, F.; Hijazi, A.; Naoufal, D.; Avalos, J. B.; Floquet, S.; Bo, C.; Cadot, E. Hydrophobic Effect as a Driving Force for Host−Guest Chemistry of a Multi-Receptor Keplerate-Type Capsule. *J. Am. Chem. Soc.* **2015**, *137*, 5845−5851.
(20) Müller, A.; Beckmann, E.; Bögge, H.; Schmidtmann, M.; Dress, A. Inorganic Chemistry Goes Protein Size: A Mo_{368} Nano-Hedgehog Initiating Nanochemistry by Symmetry Breaking. *Angew. Chem., Int. Ed.* **2002**, *41*, 1162−1167.
(21) Müller, A.; Krickemeyer, E.; Bögge, H.; Schmidtmann, M.; Peters, F. Organizational Forms of Matter: An Inorganic Super Fullerene and Keplerate Based on Molybdenum Oxide. *Angew. Chem., Int. Ed.* **1998**, *37*, 3359−3363.
(22) Sigmon, G. E.; Unruh, D. K.; Ling, J.; Weaver, B.; Ward, M.; Pressprich, L.; Simonetti, A.; Burns, P. C. Symmetry versus Minimal Pentagonal Adjacencies in Uranium-Based Polyoxometalate Fullerene Topologies. *Angew. Chem., Int. Ed.* **2009**, *48*, 2737−2740.
(23) Lin, J.; Li, N.; Yang, S.; Jia, M.; Liu, J.; Li, X.-M.; An, L.; Tian, Q.; Dong, L.-Z.; Lan, Y.-Q. Self-Assembly of Giant Mo_{240} Hollow Opening Dodecahedra. *J. Am. Chem. Soc.* **2020**, *142*, 13982−13988.
(24) Renier, O.; Falaise, C.; Neal, H.; Kozma, K.; Nyman, M. Closing Uranyl Polyoxometalate Capsules with Bismuth and Lead Polyoxocations. *Angew. Chem., Int. Ed.* **2016**, *55*, 13480−13484.
(25) Zheng, Q.; Kupper, M.; Xuan, W.; Oki, H.; Tsunashima, R.; Long, D.-L.; Cronin, L. Anisotropic Polyoxometalate Cages Assembled via Layers of Heteroanion Templates. *J. Am. Chem. Soc.* **2019**, *141*, 13479−13486.
(26) Lai, R.-D.; Zhang, J.; Li, X.-X.; Zheng, S.-T.; Yang, G.-Y. Assemblies of Increasingly Large Ln-Containing Polyoxoniobates and Intermolecular Aggregation−Disaggregation Interconversions. *J. Am. Chem. Soc.* **2022**, *144*, 19603−19610.
(27) Ma, X.-Q.; Xiao, H.-P.; Chen, Y.; Lai, Q.-S.; Li, X.-X.; Zheng, S.-T. Polyoxometalate-based macrocycles and their assembly. *Coord. Chem. Rev.* **2024**, *510*, 215818.
(28) Minato, T.; Salley, D.; Mizuno, N.; Yamaguchi, K.; Cronin, L.; Suzuki, K. Robotic Stepwise Synthesis of Hetero-Multinuclear Metal Oxo Clusters as Single-Molecule Magnets. *J. Am. Chem. Soc.* **2021**, *143*, 12809−12816.
(29) Koizumi, Y.; Yonesato, K.; Yamaguchi, K.; Suzuki, K. Ligand-Protecting Strategy for the Controlled Construction of Multinuclear Copper Cores within a Ring-Shaped Polyoxometalate. *Inorg. Chem.* **2022**, *61*, 9841−9848.
(30) Greiner, S.; Hettig, J.; Laws, A.; Baumgärtner, K.; Bustos, J.; Pöppler, A.-C.; Clark, A. H.; Nyman, M.; Streb, C.; Anjass, M. A General Access Route to High-Nuclearity, Metal-Functionalized Molecular Vanadium Oxides. *Angew. Chem., Int. Ed.* **2022**, *61*, No. e202114548.
(31) Feng, Y.; Fu, F.; Zeng, L.; Zhao, M.; Xin, X.; Liang, J.; Zhou, M.; Fang, X.; Lv, H.; Yang, G.-Y. Atomically Precise Silver Clusters Stabilized by Lacunary Polyoxometalates with Photocatalytic CO_2 Reduction Activity. *Angew. Chem., Int. Ed.* **2024**, *63*, No. e202317341.
(32) Xuan, W.; Pow, R.; Long, D.-L.; Cronin, L. Exploring the Molecular Growth of Two Gigantic Half-Closed Polyoxometalate Clusters $\{Mo_{180}\}$ and $\{Mo_{130}Ce_6\}$. *Angew. Chem., Int. Ed.* **2017**, *56*, 9727−9731.
(33) Yonesato, K.; Yanai, D.; Yamazoe, S.; Yokogawa, D.; Kikuchi, T.; Yamaguchi, K.; Suzuki, K. Surface-exposed silver nanoclusters inside molecular metal oxide cavities. *Nat. Chem.* **2023**, *15*, 940−947.
(34) Müller, A.; Shah, S. Q. N.; Bögge, H.; Schmidtmann, M. Molecular growth from a Mo_{176} to a Mo_{248} cluster. *Nature* **1999**, *397*, 48−50.
(35) Ribó, E. G.; Bell, N. L.; Long, D.-L.; Cronin, L. Engineering Highly Reduced Molybdenum Polyoxometalates via the Incorporation of d and f Block Metal Ions. *Angew. Chem., Int. Ed. Engl.* **2022**, *61*, No. e202201672.
(36) Krebs, B. Comment on molybdenum polyoxo clusters: from the Blues' to the`Reds'. *Acta Cryst. C* **2022**, *78*, 322−323.
(37) Shi, J.; Li, Y.; Jiang, X.; Yu, H.; Li, J.; Zhang, H.; Trainer, D. J.; Hla, S. W.; Wang, H.; Wang, M.; Li, X. Self-Assembly of Metallo-Supramolecules with Dissymmetrical Ligands and Characterization by Scanning Tunneling Microscopy. *J. Am. Chem. Soc.* **2021**, *143*, 1224−1234.
(38) Xu, J.; Volfova, H.; Mulder, R. J.; Goerigk, L.; Bryant, G.; Riedle, E.; Ritchie, C. Visible-Light-Driven "On"/"Off" Photochromism of a Polyoxometalate Diarylethene Coordination Complex. *J. Am. Chem. Soc.* **2018**, *140*, 10482−10487.
(39) Xuan, W.; Surman, A. J.; Miras, H. N.; Long, D.-L.; Cronin, L. Controlling the Ring Curvature, Solution Assembly, and Reactivity of Gigantic Molybdenum Blue Wheels. *J. Am. Chem. Soc.* **2014**, *136*, 14114−14120.
(40) Surman, A. J.; Robbins, P. J.; Ujma, J.; Zheng, Q.; Barran, P. E.; Cronin, L. Sizing and Discovery of Nanosized Polyoxometalate Clusters by Mass Spectrometry. *J. Am. Chem. Soc.* **2016**, *138*, 3824−3830.
(41) Huang, C.; Wang, J.-H.; Qiao, J.; Fan, X.-W.; Chen, B.; Tung, C.-H.; Wu, L.-Z. Direct Arylation of Unactivated Alkanes with Heteroarenes by Visible-Light Catalysis. *J. Org. Chem.* **2019**, *84*, 12904−12912.
(42) Quan, Y.; Lan, G.; Fan, Y.; Shi, W.; You, E.; Lin, W. Metal−Organic Layers for Synergistic Lewis Acid and Photoredox Catalysis. *J. Am. Chem. Soc.* **2020**, *142*, 1746−1751.
(43) Jin, J.; MacMillan, D. W. C. Direct α-Arylation of Ethers through the Combination of Photoredox-Mediated C-H Functionalization and the Minisci Reaction. *Angew. Chem., Int. Ed.* **2015**, *54*, 1565−1569.
(44) Holmberg-Douglas, N.; Nicewicz, D. A. Photoredox-Catalyzed C−H Functionalization Reactions. *Chem. Rev.* **2022**, *122*, 1925−2016.

https://doi.org/10.1021/jacs.4c08043
J. Am. Chem. Soc. XXXX, XXX, XXX−XXX